Observation of Spin-Tensor Induced Topological Phase Transitions of Triply Degenerate Points with a Trapped Ion

Mengxiang Zhang, 1,2,* Xinxing Yuan, 1,2,* Yue Lio, 1,2,* Xi-Wang Luo, 3,2,4,† Chang Liu, 1,2 Mingdong Zhuo, 1,2 Xi Qin, 1,2,4 Chuanwei Zhang, 5 Yiheng Lin, 1,2,4,‡ and Jiangfeng Du, 1,2,4,§

1 CAS Key Laboratory of Microscale Magnetic Resonance and School of Physical Sciences, University of Science and Technology of China, Hefei 230026, China

2 CAS Center for Excellence in Quantum Information and Quantum Physics, University of Science and Technology of China, Hefei 230026, China

3 CAS Key Laboratory of Quantum Information, University of Science and Technology of China, Hefei 230026, China

4 Hefei National Laboratory, University of Science and Technology of China, Hefei 230088, China

5 Department of Physics, The University of Texas at Dallas, Richardson, Texas 75080-3021, USA

(Received 25 January 2022; accepted 29 November 2022; published 14 December 2022)

Triply degenerate points (TDPs), which correspond to new types of topological semimetals, can support novel quasiparticles possessing effective integer spins while preserving Fermi statistics. Here by mapping the momentum space to the parameter space of a three-level system in a trapped ion, we experimentally explore the transitions between different types of TDPs driven by spin-tensor-momentum couplings. We observe the phase transitions between TDPs with different topological charges by measuring the Berry flux on a loop surrounding the gap-closing lines, and the jump of the Berry flux gives the jump of the topological charge (up to a 2π factor) across the transitions. For the Berry flux measurement, we employ a new method by examining the geometric rotations of both spin vectors and tensors, which lead to a generalized solid angle equal to the Berry flux. The controllability of a multilevel ion offers a versatile platform to study high-spin physics, and our Letter paves the way to explore novel topological phenomena therein.

DOI: 10.1103/PhysRevLett.129.250501

Introduction.—Topological states of matter, including topological insulators, and semimetals, have attracted increasing interest in the past decades [1–3]. Recent studies on topological semimetals led to the observation of Weyl [4–8] and Dirac [9,10] fermions in solid-state materials, which possess twofold or fourfold degenerate points and support relativistic spin-1/2 quasiparticles. The recent remarkable discovery of triply degenerate points (TDPs) [11–23] in fermionic systems provides an avenue for exploring new types of quasiparticles possessing integer spins while preserving Fermi statistics that have no counterparts in quantum field theory. The TDPs (i.e., threefold band degeneracies in spin-1 systems) behave like magnetic monopoles in momentum space whose topological charges \mathcal{C} are determined by the Berry flux emanating from the degenerate points. Unlike the spin-1/2 particles, a full characterization of higher spins (≥ 1) naturally involves both the spin vectors $\hat{\mathbf{F}}$ and high-rank spin tensors such as $\hat{N}_{ij} = \{\hat{F}_i, \hat{F}_j\}/2 - \delta_{ij}\hat{\mathbf{F}}^2/3 \text{ with } \{i, j\} = \{x, y, z\}. \text{ These}$ spin vectors and tensors are equivalent to the so-called Gell-Mann matrices, forming a basis of the SU(3) algebra. Therefore, an important question is to explore the roles played by spin tensors in driving the phase transition and characterizing the topologies of the TDPs.

Previous studies have predicted that spin-tensor momentum couplings can induce transitions between TDPs with different monopole charges \mathcal{C} [17–20]. On the other hand, the Berry flux and monopole charge cannot be solely determined by the solid angle of spin vector and its covering number on the Bloch sphere as in the spin-1/2 case. In fact, the spin-1 vector can go inside the Bloch sphere, and the spin tensors must also be taken into account to obtain the Berry flux [24–27].

Experimentally, TDPs with topological charge C = 2have been observed in various systems, including solidstate topological semimetal molybdenum phosphide [21] and phononic crystal [22], as well as in the synthetic parameter space of a superconducting qutrit [23]. In contrast to condensed matter systems where the realization of required spin-momentum coupling and the measurement of topological properties would be challenging, synthetic quantum systems (e.g., cold atom [28,29], superconducting qubit [30-33], nitrogen-vacancy center [34-37], trapped ion [38] systems, etc.) with versatile control offer powerful tools for the quantum simulation of topological phenomena in parameter space. To date, the topological transitions between TDPs with different monopole charges and the crucial roles played by the spin tensors have not been demonstrated experimentally.

In this Letter, by mapping the momentum space to the parameter space of a trapped ion, we experimentally explore the topological transitions between different types of TDPs and demonstrate the important roles played by the spin tensors, where the Berry flux is measured through the generalized solid angle traced out by the trajectories of both spin vectors and tensors. We simulate a momentum-space Hamiltonian

$$H = \mathbf{k} \cdot \hat{\mathbf{F}} + \alpha k_z \hat{N}_{zz} + \beta k_x \hat{N}_{xz}, \tag{1}$$

which describes the pseudospin-1 particles with a TDP at $\mathbf{k} = 0$ carrying topological charges depending on the spin-tensor-momentum coupling strengths (α, β) [39]. We effectively tune (α, β) and observe the transitions of the TDPs from C = 2 to C = 1, 0 by measuring the spin vectors and tensors. At the transitions, we observe sudden jumps of both the spin vectors (represented by arrows) and tensors (represented by ellipsoids) at the corresponding gap-closing momenta. For the transition from C=2 to C=0, the jump of topological charge is observed by measuring the Berry flux on a small loop surrounding gapclosing momenta. We adiabatically drive the system along the small loop and detect the generalized solid angle traced out by both the spin vector arrow and tensor ellipsoid, leading to a geometric phase equal to the Berry flux. Crucially, the Berry flux contains contributions from both spin vectors and tensors.

Model and experimental setup.—We consider a three-band spin-1 system with Hamiltonian given by Eq. (1). The momentum space can be parametrized by the spherical coordinates $\mathbf{k} = k_0(\sin\theta\cos\phi,\sin\theta\sin\phi,\cos\theta)$, and the TDP appears at $k_0 = 0$ where all three bands degenerate at zero energy. The bands open gaps for $k_0 > 0$ with monopole charge $\mathcal{C} = (1/2\pi) \oint \Omega_{\mathbf{k}} \cdot d\mathcal{S}$ given by the total Berry flux on the sphere \mathcal{S} surrounding the TDP [see Fig. 1(a)], where $\Omega_{\mathbf{k}} = \nabla_{\mathbf{k}} \times \mathbf{A}_{\mathbf{k}}$ and $\mathbf{A}_{\mathbf{k}} = \langle \Psi(\mathbf{k}) | i \nabla_{\mathbf{k}} | \Psi(\mathbf{k}) \rangle$ are the Berry curvature and connection respectively, and $|\Psi(\mathbf{k})\rangle$ is the eigenstate for the lowest band. The band gaps close along certain lines (i.e., gap-closing points \mathbf{k}_c are $\{\theta_c, \phi_c, \forall k_0\}$) as we change (α, β) across the phase transitions where the topological charge of the TDP changes.

A spin-1 quantum state is determined by the mean values of both spin vectors $\langle \hat{F}_i \rangle$ and tensors $\langle \hat{N}_{ij} \rangle$, which are geometrically represented by an arrow and an ellipsoid [24–27], respectively. The ellipsoid's orientation and size [see Fig. 1(b)] are determined by the eigenvectors and eigenvalues of the tensor matrix $T_{ij} = \langle \hat{N}_{ij} \rangle - \langle \hat{F}_i \rangle \langle \hat{F}_j \rangle + 2\delta_{ij}/3$ [39]. The Berry flux $\gamma = \int \Omega_{\bf k} \cdot d{\bf S}_{\mathcal L} = \oint_{\mathcal L} {\bf A}_{\bf k} \cdot d{\bf k}$ through an area ${\bf S}_{\mathcal L}$ surrounded by a loop ${\mathcal L}$ [red lines in Fig. 1(a)] can be measured by the geometric rotations of both the arrow and ellipsoid for the lowest band, where $\gamma = \gamma_F + \gamma_T$ with

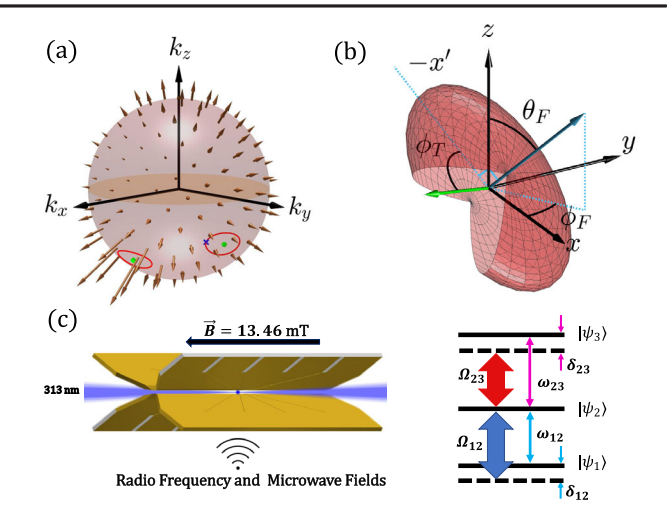


FIG. 1. Berry flux distribution, state geometric presentation, and experimental setup. (a) Berry flux distribution on momentum sphere with $\alpha=0,\beta=-1$. Green dots are the gap-closing points \mathbf{k}_c surrounded by red loops. (b) Spin tensor ellipsoid at momentum represented by the blue cross on one of the loops in (a). The longitudinal (transverse) direction of the ellipsoid is given by the spin-vector arrow in blue (short-axis arrow in green). Azimuthal angle ϕ_T of the tensor ellipsoid is given by the relative angle between the green arrow and axis -x', where x' is the rotated axis x with Euler angles $(0, \theta_F, \phi_F)$. (c) Illustration of the experimental setup, energy levels, and transitions. A three-level trapped ${}^9\mathrm{Be}^+$ ion is driven by radio frequency and microwave fields.

$$\gamma_F \equiv \oint_{\mathcal{L}} F \cos \theta_F d\phi_F \quad \text{and} \quad \gamma_T \equiv \oint_{\mathcal{L}} F d\phi_T \quad (2)$$

the generalized solid angles for the spin vector and tensor [27,39], respectively. The monopole charge (i.e., total Berry flux through S) can be obtained by sampling $S_{\mathcal{L}}$ that covers S. Topological phase transition is characterized by an abrupt change of the total Berry flux. Here F is the length of the spin-vector arrow $\langle \hat{\mathbf{F}} \rangle$, (θ_F, ϕ_F) are the spherical angles of the spin-vector arrow, ϕ_T is the relative rotation angle of the spin-tensor ellipsoid with respect to the spin-vector arrow [see Fig. 1(b)]. Therefore, the monopole charges and topological phase transitions can be characterized by the rotations of the spin-vector arrows and spin-tensor ellipsoids which can be directly detected in experiments. Notice that the Euler angles $(\phi_T, \theta_F, \phi_F)$ depend on the reference spin axis which is set as z direction here.

To simulate such a spin-1 system we map the momentum space to the parameter space of a trapped ion, whose three coupled internal states form a pseudospin-1 system. We trap a single ${}^{9}\text{Be}^{+}$ ion in a linear Paul trap [40] with ambient magnetic field of 13.46 mT [see Fig. 1(c)]. Three states, denoted as $|\psi_1\rangle$, $|\psi_2\rangle$, $|\psi_3\rangle$ respectively, in the ground manifold $2s {}^{2}S_{1/2}$ are utilized (see the Supplemental Material [39] for detailed definitions), which form the

eigenstates of \hat{F}_z in a spin-1 system, as shown in Fig. 1(c). Resonant transition frequencies between states $|\psi_i\rangle$ and $|\psi_j\rangle$ are denoted as ω_{ij} , where $\omega_{12}=2\pi\times118.966$ MHz and $\omega_{23} = 2\pi \times 991.570$ MHz. To drive these transitions, we apply impedance matched antennas [40] connected to power-amplified signal sources to induce radio frequency (RF) and microwave fields to the ion, respectively, where the former is sourced by an arbitrary wave generator (AWG) and the latter is sourced by a separate AWG, frequency-mixed with a high frequency microwave source of approximately 1 GHz. Such a configuration combining the RF and microwave transitions enables us to directly drive each transition within the ground state manifold satisfying the selection rules, and thus would be readily scalable to include more levels, particularly for demonstrations where tailored connectivity is required [41]. By programming the AWGs with the desired waveform, we apply time-dependent drives with Rabi rate Ω_{ij} , detuning δ_{ij} , and phase ϕ_{ij} , as depicted in Fig. 1. Thus in a rotating wave approximation, we obtain the desired Hamiltonian [Eq. (1)] with $\delta_{12} = (\alpha + 1)k_z = k_0(\alpha + 1)\cos\theta$, $\delta_{23} =$ $(\alpha - 1)k_z = k_0(\alpha - 1)\cos\theta$, $\Omega_{12}e^{i\phi_{12}} = (1 + \beta/2)k_x - ik_y = 0$ $(k_0 \sin \theta / \sqrt{2}) e^{-i\phi} + \beta (k_0 \sin \theta / 2\sqrt{2}) \cos \phi$ and $\Omega_{23} e^{i\phi_{23}} =$ $(1 - \beta/2)k_x - ik_y = (k_0 \sin \theta/\sqrt{2})e^{-i\phi} - \beta(k_0 \sin \theta/2\sqrt{2}) \times$ $\cos \phi$. Here, k_0 only modifies the magnitudes of the energy bands without affecting the eigenstates; therefore, we focus our discussions on a sphere with fixed k_0 .

The experiment begins with a series of controlled 313 nm laser beam pulses [Fig. 1(c)] to Doppler cool the ion motion and initialize it to $|\psi_2\rangle$ to further couple to the other states. We then apply a sequence of resonant RF and microwave pulses to prepare the ion to the ground state of the Hamiltonian for given parameters $\{\alpha, \beta, \theta, \phi\}$, where the amplitudes and durations of the control pulses can be calculated via diagonalizing the Hamiltonian. To measure the Berry flux within a loop, we subsequently apply an adiabatic ramp of the parameters (θ, ϕ) along the loop of interest on the sphere with fixed α and β . We stop the evolution at various points on the loop, and measure the observables $\langle \hat{F}_i \rangle$, $\langle \hat{N}_{ij} \rangle$ [39].

Observation of the topological phase transitions.—We first set $\beta=0$ and consider the transition from $\mathcal{C}=2$ to $\mathcal{C}=1$ by increasing α . The first (second) band gap closes at the north (south) pole $\theta_c=0$ ($\theta'_c=\pi$) on the momentum sphere respectively, as α changes across $\alpha_c=1$. We measure the corresponding spin vectors $\langle \hat{F}_i \rangle$ and tensors $\langle \hat{N}_{ij} \rangle$ of the ground state at $\theta=0$ for different α . As depicted in Fig. 2, the measured value of $\langle \hat{F}_z \rangle$ for $\alpha<1$ is approximately equal to -1 but dramatically jumps to approximately 0 when $\alpha>1$ ($\langle \hat{F}_x \rangle$ and $\langle \hat{F}_y \rangle$ are always approximately equal to 0), indicating a phase transition. As also depicted in Fig. 2, we observe a dramatic change of ellipsoid around the phase transition $\alpha=1$. Moreover, we observe the spin vortex at the north pole for $\alpha>1$ [39],

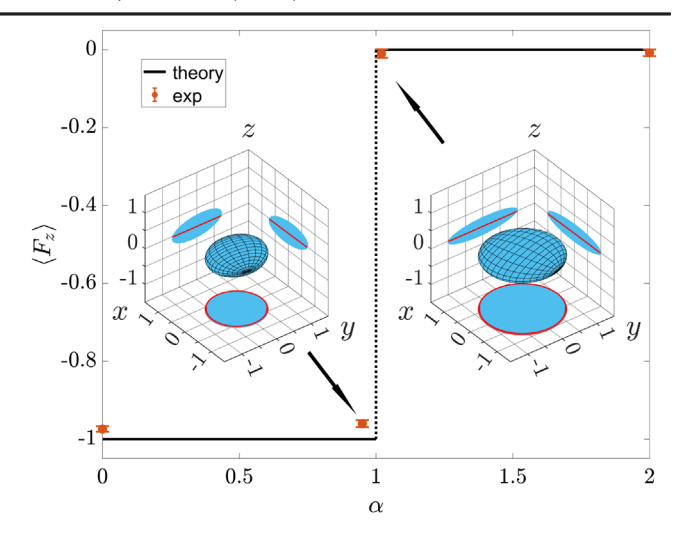


FIG. 2. Phase transition characterized by the jump of spin vector and tensor. Error bars correspond to 1 standard deviation. Insets: tensor ellipsoids and their projection on the x, y, and z plane at $\alpha=0.95$ (left with $\mathcal{C}=2$) and $\alpha=1.05$ (right with $\mathcal{C}=1$), with $\beta=0$. The red circles and lines are the projections of the theoretical tensor ellipsoids. The experimental imperfection leads to a finite axis length of the ellipsoid along the z direction ~ 0.3 , corresponding to a bias of $0.3^2 \sim 10\%$ in measuring \hat{N}_{ij} .

which also signals the transition of the monopole charge [18]. To illustrate the jump of monopole charge, we examine latitude loops on the momentum sphere since the Hamiltonian has cylindrical symmetry with respect to the z axis, leading to $\gamma_F = -2\pi \cdot \langle \hat{F}_z \rangle$ [39]. The tensor has no contribution to the Berry flux where ϕ_T is always 0 in the case of $\beta=0$. From Fig. 2, we observe $\langle \hat{F}_z \rangle$ approximately changes by 1 at the north pole $\theta=0$, matching with the expected 2π change of the Berry flux, and thus the monopole charge $\mathcal{C}=\langle \hat{F}_z \rangle|_{\theta=0}^{\theta=\pi}$ changes by 1.

In general, both the vectors and tensors should contribute to the Berry flux for a spin-1 model. To show this, we examine the topological phase transition from $\mathcal{C}=2$ to $\mathcal{C}=0$ and set $\alpha=0,\ \beta\neq0$ for a different spin-tensor-momentum coupling. We notice that at the vicinity of the phase transition, the sudden change of the monopole charge must be given by the sudden change of the Berry flux near the nonanalytical point (i.e., the gap-closing point). Therefore, measuring the Berry flux near the gap-closing point can be used to probe the topological phase transition directly. The first (second) band gap closes at $(\theta_c,\phi_c)=(3\pi/4,0)$ and $(3\pi/4,\pi)$ $[(\theta'_c,\phi'_c)=(\pi/4,0)$ and $(\pi/4,\pi)]$ on the momentum sphere across the phase transition point $\beta_c=-2$. We observe jumps of both spin vectors and tensors at the transition [39].

To measure the change of monople charge, we consider small loops [solid lines in Fig. 1(a)] on the momentum sphere surrounding the gap-closing point. After the ground state preparation of the initial Hamiltonian, we evolve the

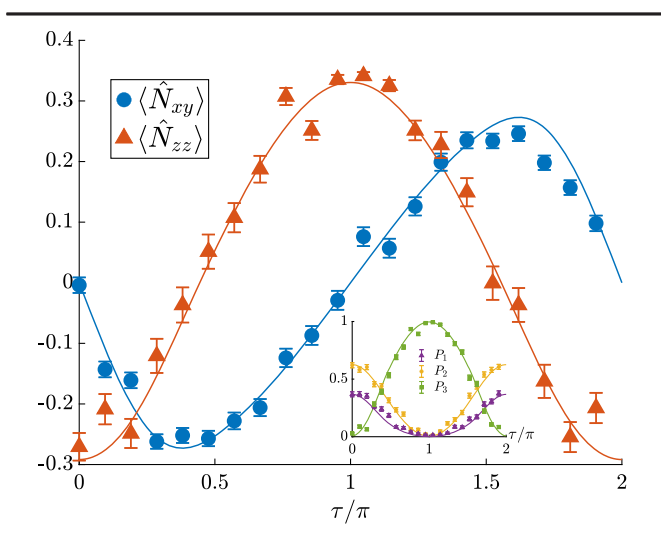


FIG. 3. Measured spin tensors at different position τ along the loop \mathcal{L} with $\alpha=0,\beta=-1.9$. Blue circles and red triangles are $\langle \hat{N}_{xy} \rangle$ and $\langle \hat{N}_{zz} \rangle$ respectively (more data can be found in the Supplemental Material [39]). In the inset, green squares, yellow circles, and purple triangles show the populations $P_{i=\{1,2,3\}}$ respectively for the eigenstates of \hat{N}_{zz} . Error bars correspond to 1 standard deviation. Solid lines represent the corresponding numerical simulations.

state by subsequently applying an adiabatic ramp of the parameters along the loop \mathcal{L} : $\theta = (3\pi/4) - (3/4)r\cos\tau$ and $\phi = \pi - \sqrt{3}r \sin \tau$ with a nearly uniform gap, where we ramp τ from 0 to 2π with a constant rate. By programming separate channels of the AWG and setting $\tau = 2\pi t/T$, we generate the desired time-dependent Hamiltonian along the loop [39], with T the maximum ramp time of 1 ms. We choose r = 0.2, and the ramp rate is separately checked via a numerical simulation to ensure a required level of adiabaticity and coherence [39]. We observe a number of $\langle \hat{F}_i \rangle$, $\langle \hat{N}_{ij} \rangle$ at various τ (see Fig. 3 for $\beta = -1.9$ as an example) by measuring the eigenstate populations of these observables, from which we obtain the spin-vector length F, the Euler angles ϕ_T , θ_F , ϕ_F . Finally, we arrive at the Berry phase $\gamma = \gamma_F + \gamma_T$. By repeatedly measuring the Berry flux over a selection of β , we observe the Berry flux changes from 0 at $|\beta + 2| \gg 0$ to approximately $\pm \pi$ at $|\beta + 2| = 0$, with a sharp transition by 2π at $\beta = -2$ [see Fig. 4(a)]. Similarly, one could apply measurement of the Berry flux on the loop around $\theta_c = 3\pi/4, \phi_c = 0$, and the Berry flux should also change by 2π . Thus, the monople charge must change by 2 across the phase transition at $\beta_c = -2$, i.e., C changes from 2 to 0.

Ideally, we should consider an infinitely small loop $r \approx 0$ to obtain a sharp transition exactly at $\beta = -2$; however, such an evolution requires an infinitely slow ramp rate and measurement resolution, thus rendering it not feasible in practice. Nevertheless, a finite size loop with r = 0.2 is good enough to show the phase transition. For a finite but

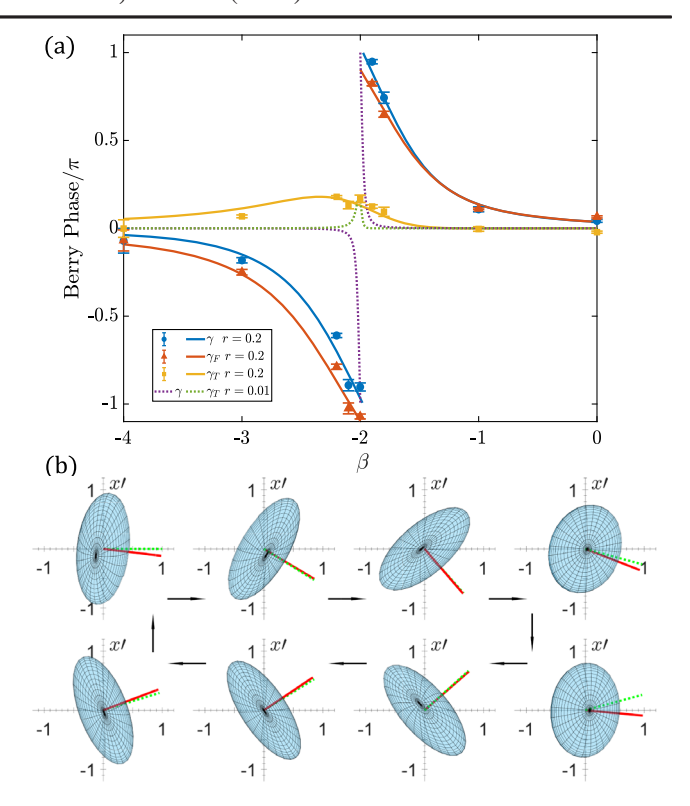


FIG. 4. Berry flux and trajectory of corresponding ellipsoids. (a) Berry flux γ through the loop \mathcal{L} versus β . Blue circles, red triangles, and yellow squares are the experimental data of γ , γ_F , and γ_T respectively with r=0.2; the solid lines are the corresponding numerical simulations in the adiabatic limit. Purple and green dashed lines are the numerical simulations of γ and γ_T with r=0.01 respectively. Error bars correspond to 1 standard deviation. (b) Measurements of the tensor ellipsoids along the adiabatic loop at $\beta=-2.2$, with $\tau=\{0,0.19,0.48,0.95,1.05,1.71,1.81,1.90\}\pi$ starting from the top left along the direction indicated by black arrows. The red solid (green dashed) lines represent the direction of the short axis of the ellipsoid from experimental data (numerical simulations), showing the evolution of ϕ_T and the rotation with respect to $\langle \hat{\mathbf{F}} \rangle$.

small loop, the Berry flux is also small unless there is a nonanalytical gap-closing point within the loop, so we can restrict the Berry flux to $[-\pi, \pi]$, and the jump between $\pm \pi$ gives the critical point. Such a jump for r=0.2 can be seen around $\beta=-1.98$ in the numerical simulation, away from which, the Berry flux changes smoothly, as shown in Fig. 4(a).

We plot and observe relative rotations of the tensor ellipsoid with respect to the spin vector along the loop \mathcal{L} with $\beta=-2.2$, as illustrated in Fig. 4(b), and the direction of tensor ellipsoids are more sensitive to experimental noises when the two transverse axes have similar length. We find ϕ_T undergoes a sinelike oscillation along the loop while F undergoes a cosinelike oscillation. Such rotation gives a nontrivial spin-tensor contribution $\oint_{\mathcal{L}} F d\phi_T \simeq 0.18\pi$ for the Berry flux around the phase transition. For the phase transition with $\beta \neq 0$, both the spin vectors and

tensors contribute to the Berry flux, independent from the choice of reference axis defining the Euler angles. Though different choices (with quantum states related by gauge transformations) will modify $(\phi_T, \theta_F, \phi_F)$ and thereby γ_F and γ_T , γ remains invariant. For systems with certain symmetries (e.g., the cylindrical symmetry), it is possible to eliminate γ_T by proper choice of the reference axis [39]. By now we have demonstrated the topological phase transition by measuring the sudden change of the Berry flux. To visualize the monopole at $k_0 = 0$, we can measure the total Berry flux on the sphere \mathcal{S} based on generalized solid angles. Alternatively, a distribution of spin polarization $\langle \hat{\mathbf{F}} \rangle$ on the sphere can also be used to visualize a monopole, as demonstrated in the Supplemental Material [39].

Conclusion.—In summary, we experimentally explore the momentum-space spin-1 Hamiltonian and observe the tensor-driven transitions between different types of TDPs with a trapped ion. By examining the vector arrow and tensor ellipsoid properties around the gap-closing points, we experimentally observe the transitions between different monopole charges of the TDP. Our Letter demonstrates the feasibility of measuring Berry flux of high-spin systems based on the generalized solid angle traced out by the spin moments (vectors and tensors) which can apply to general three-band systems, paving the way for exploring topological phenomena directly from the geometric rotations of the spin moments in such systems. Moreover, our study can be generalized to explore topological phenomena such as triply degenerate points with larger monopole charges and higher-order dispersions [19,20,42] as well as higher-fold degenerate points [43], since we have full control of the detunings, couplings of the three levels and our setup may be readily scaled to more levels based on our experimental techniques for ⁹Be⁺ ion, which can be extended to more ions with multiple levels therein [44–46].

The USTC team acknowledges support from the National Natural Science Foundation of China (Grants No. 92165206 and No. 11974330), the Chinese Academy of Sciences (Grant No. XDC07000000), Innovation Program for Quantum Science and Technology (Grants No. 2021ZD0301603 and No. 2021ZD0301200), Anhui Initiative in Quantum Information Technologies (Grant No. AHY050000), the USTC start-up funding, and the Fundamental Research Funds for the Central Universities, and Hefei Comprehensive National Science Center. C. Z. is supported by the National Science Foundation (PHY-2110212).

- [2] M. Z. Hasan and C. L. Kane, Rev. Mod. Phys. 82, 3045 (2010).
- [3] X.-L. Qi and S.-C. Zhang, Rev. Mod. Phys. 83, 1057 (2011).
- [4] X. Wan, A. M. Turner, A. Vishwanath, and S. Y. Savrasov, Phys. Rev. B 83, 205101 (2011).
- [5] M. Hirschberger, S. Kushwaha, Z. Wang, Q. Gibson, S. Liang, C. A. Belvin, B. A. Bernevig, R. J. Cava, and N. P. Ong, Nat. Mater. 15, 1161 (2016).
- [6] B. Q. Lv, H. M. Weng, B. B. Fu, X. P. Wang, H. Miao, J. Ma, P. Richard, X. C. Huang, L. X. Zhao, G. F. Chen, Z. Fang, X. Dai, T. Qian, and H. Ding, Phys. Rev. X 5, 031013 (2015).
- [7] S.-Y. Xu, I. Belopolski, N. Alidoust, M. Neupane, G. Bian, C. Zhang, R. Sankar, G. Chang, Z. Yuan, C.-C. Lee, S.-M. Huang, H. Zheng, J. Ma, D. S. Sanchez, B. Wang, A. Bansil, F. Chou, P. P. Shibayev, H. Lin, S. Jia, and M. Z. Hasan, Science 349, 613 (2015).
- [8] L. Lu, Z. Wang, D. Ye, L. Ran, L. Fu, J. D. Joannopoulos, and M. Soljačić, Science 349, 622 (2015).
- [9] J. Xiong, S. K. Kushwaha, T. Liang, J. W. Krizan, M. Hirschberger, W. Wang, R. J. Cava, and N. P. Ong, Science 350, 413 (2015).
- [10] Z. K. Liu, B. Zhou, Y. Zhang, Z. J. Wang, H. M. Weng, D. Prabhakaran, S.-K. Mo, Z. X. Shen, Z. Fang, X. Dai, Z. Hussain, and Y. L. Chen, Science 343, 864 (2014).
- [11] B. Bradlyn, J. Cano, Z. Wang, M. G. Vergniory, C. Felser, R. J. Cava, and B. A. Bernevig, Science 353, aaf5037 (2016).
- [12] H. Yang, J. Yu, S. S. P. Parkin, C. Felser, C.-X. Liu, and B. Yan, Phys. Rev. Lett. 119, 136401 (2017).
- [13] H. Weng, C. Fang, Z. Fang, and X. Dai, Phys. Rev. B 93, 241202(R) (2016).
- [14] Z. Zhu, G. W. Winkler, Q. S. Wu, J. Li, and A. A. Soluyanov, Phys. Rev. X 6, 031003 (2016).
- [15] C. Zhong, Y. Chen, Z.-M. Yu, Y. Xie, H. Wang, S. A. Yang, and S. Zhang, Nat. Commun. 8, 15641 (2017).
- [16] I. C. Fulga, L. Fallani, and M. Burrello, Phys. Rev. B 97, 121402(R) (2018).
- [17] H. Hu, J. Hou, F. Zhang, and C. Zhang, Phys. Rev. Lett. **120**, 240401 (2018).
- [18] H. Hu and C. Zhang, Phys. Rev. A 98, 013627 (2018).
- [19] X.-Y. Mai, Y.-Q. Zhu, Z. Li, D.-W. Zhang, and S.-L. Zhu, Phys. Rev. A 98, 053619 (2018).
- [20] Zhoutao Lei, Yuangang Deng, and Chaohong Lee, Phys. Rev. Res. 4, 033008 (2022).
- [21] B. Q. Lv, Z.-L. Feng, Q.-N. Xu, X. Gao, J.-Z. Ma, L.-Y. Kong, P. Richard, Y.-B. Huang, V. N. Strocov, C. Fang, H.-M. Weng, Y.-G. Shi, T. Qian, and H. Ding, Nature (London) 546, 627 (2017).
- [22] Y. Yang, H.-X. Sun, J.-P. Xia, H. Xue, Z. Gao, Y. Ge, D. Jia, S.-Q. Yuan, Y. Chong, and B. Zhang, Nat. Phys. 15, 645 (2019).
- [23] X. Tan, D.-W. Zhang, Q. Liu, G. Xue, H.-F. Yu, Y.-Q. Zhu, H. Yan, S.-L. Zhu, and Y. Yu, Phys. Rev. Lett. 120, 130503 (2018)
- [24] H. M. Bharath, J. Math. Phys. (N.Y.) 59, 062105 (2018).
- [25] H. M. Bharath, M. Boguslawski, M. Barrios, L. Xin, and M. S. Chapman, Phys. Rev. Lett. 123, 173202 (2019).
- [26] X. Zhou, X.-W. Luo, G. Chen, S. Jia, and C. Zhang, Phys. Rev. B **101**, 140412(R) (2020).

These authors contributed equally.

[†]luoxw@ustc.edu.cn

[‡]yiheng@ustc.edu.cn

[§]djf@ustc.edu.cn

^[1] A. H. Castro Neto, F. Guinea, N. M. R. Peres, K. S. Novoselov, and A. K. Geim, Rev. Mod. Phys. 81, 109 (2009).

- [27] X.-W. Luo and C. Zhang, Phys. Rev. A 102, 033339 (2020).
- [28] S. Sugawa, F. Salces-Carcoba, A. R. Perry, Y. Yue, and I. B. Spielman, Science **360**, 1429–1434 (2018).
- [29] Q.-X. Lv, Y.-X. Du, Z.-T. Liang, H.-Z. Liu, J.-H. Liang, L.-Q. Chen, L.-M. Zhou, S.-C. Zhang, D.-W. Zhang, B.-Q. Ai, H. Yan, and S.-L. Zhu, Phys. Rev. Lett. 127, 136802 (2021).
- [30] P. Roushan, C. Neill, Y. Chen, M. Kolodrubetz, C. Quintana, N. Leung, M. Fang, R. Barends, B. Campbell, Z. Chen, B. Chiaro, A. Dunsworth, E. Jeffrey, J. Kelly, A. Megrant, J. Mutus, P. J. J. OMalley, D. Sank, A. Vainsencher, J. Wenner, T. White, A. Polkovnikov, A. N. Cleland, and J. M. Martini, Nature (London) 515, 241 (2014).
- [31] M. D. Schroer, M. H. Kolodrubetz, W. F. Kindel, M. Sandberg, J. Gao, M. R. Vissers, D. P. Pappas, A. Polkovnikov, and K. W. Lehnert, Phys. Rev. Lett. 113, 050402 (2014).
- [32] X. Tan, D.-W. Zhang, Z. Yang, J. Chu, Y.-Q. Zhu, D. Li, X. Yang, S. Song, Z. Han, Z. Li, Y. Dong, H.-F. Yu, H. Yan, S.-L. Zhu, and Y. Yu, Phys. Rev. Lett. 122, 210401 (2019).
- [33] X. Tan, D.-W. Zhang, W. Zheng, X. Yang, S. Song, Z. Han, Y. Dong, Z. Wang, D. Lan, H. Yan, S.-L. Zhu, and Y. Yu, Phys. Rev. Lett. 126, 017702 (2021).
- [34] F. Kong, C. Ju, Y. Liu, C. Lei, M. Wang, X. Kong, P. Wang, P. Huang, Z. Li, F. Shi, L. Jiang, and J. Du, Phys. Rev. Lett. 117, 060503 (2016).
- [35] W. Ma, L. Zhou, Q. Zhang, M. Li, C. Cheng, J. Geng, X. Rong, F. Shi, J. Gong, and J. Du, Phys. Rev. Lett. 120, 120501 (2018).

- [36] W. Ji, L. Zhang, M. Wang, L. Zhang, Y. Guo, Z. Chai, X. Rong, F. Shi, X.-J. Liu, Y. Wang, and J. Du, Phys. Rev. Lett. 125, 020504 (2020).
- [37] X.-X. Yuan, L. He, S.-T. Wang, D.-L. Deng, F. Wang, W.-Q. Lian, X. Wang, C.-H. Zhang, H.-L. Zhang, X.-Y. Chang, and L.-M. Duan, Chin. Rev. Lett. 34, 060302 (2017).
- [38] D. Leibfried, R. Blatt, C. Monroe, and D. Wineland, Rev. Mod. Phys. 75, 281 (2003).
- [39] See Supplemental Materials at http://link.aps.org/supplemental/10.1103/PhysRevLett.129.250501 for details about the model and phase diagram, the geometric representation of the spin-1 quantum state and Berry phase, the experimental setup, detecting method, and experimental data for the measurement of spin vectors and tensors.
- [40] Y. Li, Z.-C. He, X. Yuan, M. Zhang, C. Liu, Y.-X. Wu, M. Zhu, X. Qin, Z.-Y. Xue, Y. Lin, and J. Du, Phys. Rev. Appl. 18, 034047 (2022).
- [41] M. W. Ray, E. Ruokokoski, S. Kandel, M. Möttönen, and D. S. Hall, Nature (London) 505, 657 (2014).
- [42] S. Nandy, S. Manna, D. Călugăru, and B. Roy, Phys. Rev. B 100, 235201 (2019).
- [43] L. Liang and Y. Yu, Phys. Rev. B 93, 045113 (2016).
- [44] P. J. Low, B. M. White, A. A. Cox, M. L. Day, and C. Senko, Phys. Rev. Res. 2, 033128 (2020).
- [45] Y. Wang, Z. Hu, B. C. Sanders, and S. Kais, Front. Phys. 8, 589504 (2020).
- [46] M. Ringbauer, M. Meth, L. Postler, R. Stricker, R. Blatt, P. Schindler, and T. Monz, Nat. Phys. 18, 1053 (2022).